CrossMark

Electrical conductivity of hydrous natural basalts at high temperatures and pressures

Lidong Dai [a,*], Jianjun Jiang [a,b], Heping Li [a], Haiying Hu [a], Keshi Hui [a,b]

[a] Key Laboratory of High-Temperature and High-Pressure Study of the Earth's Interior, Institute of Geochemistry, Chinese Academy of Sciences, Guiyang, Guizhou 550002, China
[b] Graduate School of Chinese Academy of Sciences, Beijing 100039, China

ARTICLE INFO

ABSTRACT

The electrical conductivities of natural iron-bearing basalts, with a water content ranging from 0.62 to 4.19 wt.%, were determined for a range of pressure (0.5–2.0 GPa) and temperature (823–1173 K) conditions. A Ni–NiO solid oxygen buffer was selected to stabilize the oxygen partial pressure. Increasing pressure causes the electrical conductivity of the hydrous sample to slightly decrease, whereas the activation enthalpy increases. The activation energy and activation volume are 0.86 ± 0.14 eV and 1.43 ± 0.25 cm^3/mol, respectively. At a constant pressure of 2.0 GPa, the electrical conductivity increases with increasing water content. Considering the dependence of activation enthalpy on water content for all samples at 2.0 GPa, the electrical conductivity data were fitted to the formula $\sigma = \left(A_1 + A_2 * C_w^{\gamma} \right) * \exp\left(\frac{-\Delta H_0 - \alpha C_w^{\beta}}{RT} \right)$, where A_1 and A_2 is the pre-exponential factor, C_W is the water content in sample, ΔH_0 is the activation enthalpy at very low water concentrations, T is the absolute temperature, k is the Boltzmann constant, and r, α and β are constants. Furthermore, the electrical conductivity of natural hydrous basalts cannot account for the crustal high-conductivity anomaly observed in magnetotelluric results observed in the North China Craton, Axial Volcanic Ridge, and Transverse Electric models.

© 2014 Elsevier B.V. All rights reserved.

1. Introduction

Magnetotelluric (MT) surveying is a powerful tool for mapping anomalous conductive zones, such as magma conduits in volcanic settings, to evaluate their subaerial extent and infer their chemical properties (Bagdassarov and Delépine, 2004; Bagdassarov et al., 2009, 2011; Parkhomenko and Bondarenko, 1986; Selway, 2014). However, since electromagnetic methods yield non-unique solutions, experimental observations of the electrical properties of minerals and rocks provide critical information for the quantitative interpretation of MT data to image the structure and composition of the earth's interior (Bedrosian, 2007; Selway et al., 2014; Tyburczy and Waff, 1983). Thus, experimental constraints on the electrical conductivity of deep earth materials are essential for characterizing crust and mantle structure via electromagnetic methods.

Recent experimental results have identified partial melt and hydrogen content in minerals and rocks as the key parameters that cause conductivity anomalies in the asthenosphere and lower continental crust (Dai and Karato, 2014; Dai et al., 2014; Ni et al., 2011; Yang et al., 2011, 2012). Electrical conductivity measurements on both dry and hydrous basaltic melt have been extensively conducted under defined thermodynamic conditions, although the degree of melt fraction required to produce the observed conductivity anomalies remains debated (Maumus et al., 2005; Pommier et al., 2010; Tyburczy and Waff, 1983). However, constraints on the electrical conductivity of natural hydrous basalts at high temperatures (T) and pressures (P) are limited. Scarlato et al. (2004) measured the electrical conductivity of basaltic rocks as a function of partial melting at high temperature and pressure, assuming an anhydrous state, and observed that the conductivity can increase by as much as a factor of 3 with increasing melt fraction. Ni et al. (2011) examined the electrical conductivity of both H_2O- and CO_2-bearing synthetic basaltic melts at $P = 2.0$ GPa and $T = 1473$–1923 K, reporting that 2 vol% of melt can produce the observed conductivity anomaly in the seismic low-velocity zone. A systemic study exploring the influence of temperature, pressure, and water content (Wc) on the electrical conductivity of natural hydrous basalts is thus necessary to better quantify the degree of melt in rocks and to interpret high-conductivity anomalies in MT data.

In this study, we measured the electrical conductivity of natural iron-bearing basalt samples for a range of water contents, $P = 2.0$ GPa, and $T = 823$–1173 K, by means of complex impedance spectroscopy in a multi-anvil apparatus. The conductivity measurement of one sample was carried out at $P = 0.5$–2.0 GPa and $T = 823$–1173 K to examine the effect of pressure and water content on the bulk conductivity of hydrous basalts. The geophysical implications for the application of these results to establish a laboratory-based conductivity–depth profile was discussed.

* Corresponding author. Tel.: +86 851 5891424; fax: +86 851 5891749.
  E-mail address: dailidong717@hotmail.com (L. Dai).

2. Experimental procedures

2.1. Sample description

Four natural basalts, each with a different chemical composition, were chosen from Hannuoba, in north China (XW-1); Deqin, in Yunnan province (XW-3); Emeishan, in Sichuan province (XW-5) and Gejiu, in Yunnan province (XW-7). These samples are fresh, non-fractured, non-oxidized, and contain both clinopyroxene and plagioclase phenocrysts. A PANalytical Axios-Advance (Axios PW4400) X-ray fluorescence spectrometer (XRF) was employed to determine the chemical compositions of the samples and the results are listed in Table 1. The XRF samples were pulverized and fused to a glass disk, and the XRF analysis was conducted across a broad element distribution, ranging from beryllium to uranium, yielding a ppb% analytic concentration of each element; the XRF has a 2-minute IQ-fast scanning speed, producing analysis errors of <5%. Loss on ignition (LOI) was obtained for each sample by heating 1 g of powder to 1373 K for 1 h. For full details of the XRF analysis procedure, see Liu et al. (2012). To confirm the phase state of each sample during the electrical conductivity measurements, a quenched Hannuoba basalt image was taken after the electrical conductivity measurements with an optical microscope in plane-polarized reflected light, as shown in Fig. 1(a). Representative back-scattered electron images were also taken to verify the phase state, using both an electron microscope and scanning electronic microscope, as illustrated in Fig. 1(b) and (c). These results confirmed that a phase transition was not observed during the conductivity experiments.

The iron content of the basalt samples (XW-1, XW-3, XW-5, and XW-7 were composed of $X_{Fe} = Fe^{\#}(\%) = \sum Fe/(Mg + \sum Fe + Ca) = $ 25.31, 28.57, 30.31 and 31.96%, respectively) is very close to the chemical composition of typical Mesozoic primitive basalts from the North China Craton (Xia et al., 2013). The basalt samples were cut and polished into a cylinder with a diameter of 6.0 mm and a height of 6.0 mm, using an ultrasonic drill and diamond saw; the samples were then cleaned with deionized distilled water, alcohol, and acetone in turn. Finally, all of the samples were heated for 48 h in a 473 K vacuum drying oven to remove any adsorbed water from the sample surfaces.

In order to determine the water content in basalt samples, we have conducted the secondary ion mass spectrometry (SIMS) analysis, and our obtained water contents for four basalt samples are 0.62, 1.59, 2.74 and 4.19 wt.%, respectively.

2.2. High-pressure conductivity cell and impedance measurements

High-pressure electrical conductivity measurements were performed in the YJ-3000t multi-anvil apparatus and a Solartron-1260A Impedance/Gain-Phase Analyzer. We employed the same measurement techniques and experimental procedures as those outlined by Li et al. (1999) and Hu et al. (2011, 2013).

Fig. 2 shows the experimental assemblage for the electrical conductivity measurements. High pressures were generated by six cubic tungsten carbide anvils with a 23.4 mm surface length. The sample chamber pressure was calibrated from the Cu, Al, Zn, and Pb melting curves, and from a 3D polynomial numerical fitting for $P = 1.0$–5.0 GPa and $T = 662$–1518 K (Shan et al., 2007). Temperature calibrations were made by measuring the ultrasonic wave velocities for window

glass, pyrophyllite, and kimberlite at $P = 0.1$–5.5 GPa and $T = 409$–1673 K (Xu et al., 1994). The pressure medium of pyrophyllite ($32.5 \times 32.5 \times 32.5$ mm^3) was baked at 973 K for 2 h prior to the electrical conductivity experiments. A grounded Faraday shielding case of 0.05 mm nickel foil was installed between the aluminum oxide (Al_2O_3) and boron nitride (BN) insulation sleeve to reduce the temperature gradient inside the sample cell, to minimize current leakage across the pressure medium, to prevent chemical migration between the sample and the pressure medium, and to control the oxygen partial pressure. A cylindrical sample ($d = 6.0$ mm and $h = 6.0$ mm) was placed in the middle of the BN insulation sleeve and sandwiched by two symmetrical nickel electrodes, as Fuji-ta et al. (2004) noted that BN can provide a higher insulation than Al_2O_3 during electrical conductivity measurements of minerals and rocks at high temperatures and pressures. Here the BN insulation sleeve is employed to decrease the oxygen fugacity for the solid Ni–NiO buffer; however, according to our previous studies, the effect of oxygen fugacity on the electrical conductivity of crustal and upper-mantle minerals and rocks is small in comparison with the effect of water content (Dai et al., 2012, 2013). Temperature was monitored using a NiCr–NiAl thermocouple. Measurement errors derived from the pressure and temperature gradients were less than 0.1 GPa and 10 K, respectively.

Pressure was slowly increased at a rate of 0.90 GPa/h to the desired value during the experiment. Temperature was then gradually increased at a rate of 120 K/h to the designated values. Once the designated pressure and temperature were reached for each run, the temperature was changed in 50 K intervals, and the impedance spectroscopy of the sample was measured using a Solartron-1260A Impedance/Gain-Phase Analyzer with a sinusoidal signal voltage of 1.0 V in the 10^{-2} to 10^6 Hz frequency range. Temperature was held constant for a few minutes at each step to ensure the thermal transfer in the sample cell reached equilibrium, and to obtain a steady impedance spectroscopy. The complex impedance spectra of the XW-1 sample were collected in two heating-cooling cycles to assess the reproducibility of the electrical conductivity measurements; the impedance spectra were only collected over one heating–cooling cycle for the other samples. The sample resistance was obtained by using an equivalent circuit, composed of a resistance (R) and capacitance (C), in parallel to fit the experimental data. The conductivity of the samples was then calculated from the sample resistance and the dimensions of the recovered samples after each run. A representative recovered experimental assembly after electrical conductivity for the XW-1 basalt at $P = 2.0$ GPa is illustrated in Fig. 3. The electrical conductivity measurement errors were estimated to be less than 5%, derived mainly from the fitting error of impedance semicircular arcs and the dimensional distortion of the sample during the experimental process.

3. Results

We measured the electrical conductivities of: (1) the XW-1 Hannuoba basalt over two heating–cooling cycles at $P = 2.0$ GPa; (2) the XW-1 Hannuoba basalt at $P = 0.5$–2.0 GPa and $T = 823$–1173 K; and (3) all basalt samples, with varying water contents ($Cw = 0.62, 1.59, 2.74,$ and 4.19 wt.%) at $P = 2.0$ GPa and $T = 823$–1173 K. The frequency range of the impedance spectra is 10^{-2} to 10^6 Hz.

Table 1
Chemical composition (X-ray fluorescence) for the starting materials.

Sample No	SiO₂	Al₂O₃	FeO	MgO	CaO	Na₂O	K₂O	MnO	P₂O₅	TiO₂	LOI	Fe#	Total
XW-1	41.12	11.09	12.74	16.04	7.03	1.63	1.83	0.14	0.69	2.44	6.47	25.31	101.22
XW-3	52.23	16.1	9.75	7.56	8.51	3.39	0.6	0.17	0.17	1.44	0.01	28.57	99.92
XW-5	50.68	16.14	10.74	7.44	8.92	3.51	0.65	0.18	0.17	1.51	0.01	30.31	99.94
XW-7	49.08	15.13	11.33	7.35	8.60	3.49	0.59	0.18	0.17	1.47	3.20	31.96	100.59

Note: LOI, loss on ignition. Fe# = $100 \times \Sigma Fe/(Mg + \Sigma Fe + Ca)$.
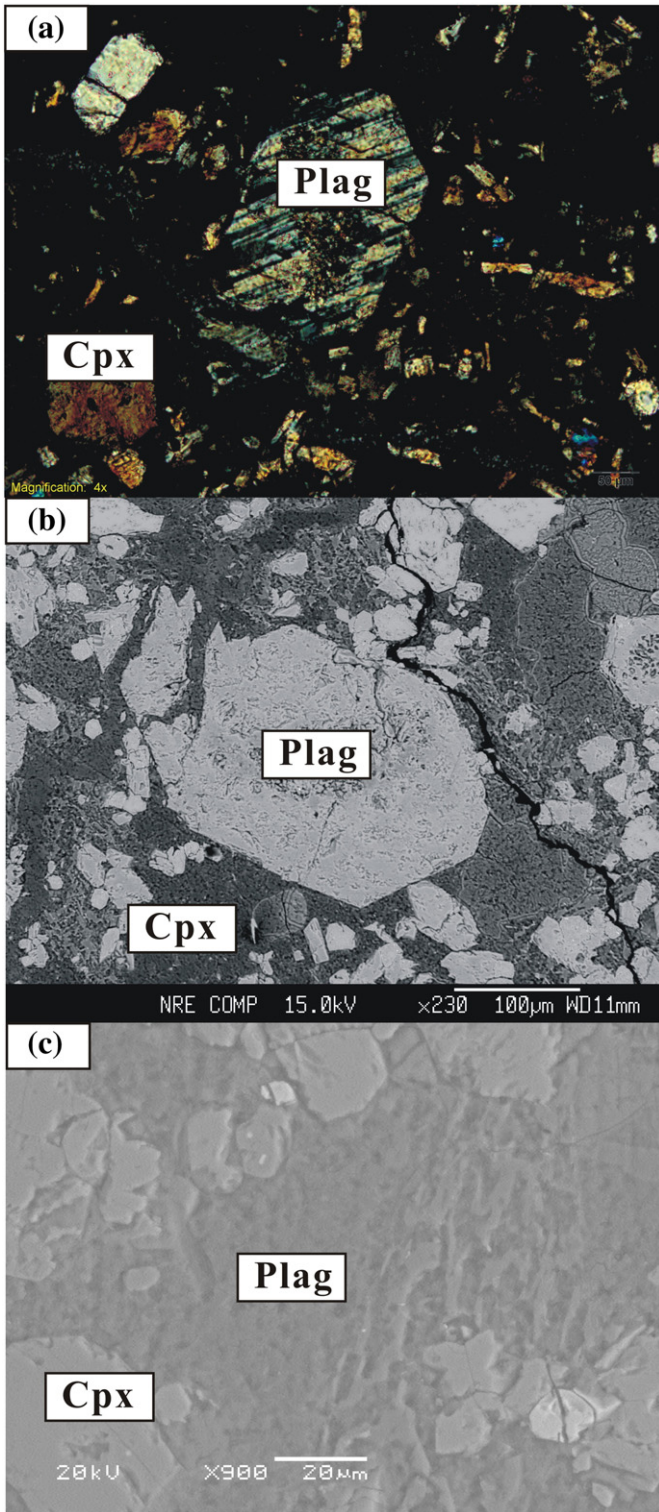
Fig. 1. Experimental production in the sample of run XW-1 shown in the microscopic image derived from the plane-polarized reflected light and the back-scattered electron images from the analysis of electron microscope and scanning electronic microscope. Abbreviations are clinopyroxene (Cpx) and plagioclase (Plag), respectively.

The representative complex impedance spectra for $P = 2.0$ GPa and $T = 823$–1173 K are illustrated in Fig. 4. In most cases, the spectra show one semicircular arc in the higher-frequency range and an additional tail at lower frequencies, as previously reported for polycrystalline minerals and rocks (Huebner and Dillenburg, 1995; Roberts and Tyburczy, 1991; Watson et al., 2010). As temperature increases, the diameter of

the impedance arc decreases due to the decrease in relaxation time associated with the charge transport process, indicating that the sample becomes more conductive. Impedance spectroscopy theory states that an electrode response in the complex impedance plane can appear either as a separate or overlapping impedance arc or as a straight line, which is characteristic of diffusion processes at the sample–electrode interface (Bagdassarov, 2011; Gasc et al., 2011; Hu et al., 2014). Thus, we use only the first arcs, which represent the bulk electrical properties of the sample, to determine the conductivity of the sample. An equivalent circuit consisting of the RC in parallel, as shown in Fig. 4, is chosen to fit the impedance semicircles and obtain the sample resistance. The electrical conductivity of the sample is then calculated as

$$\sigma = \frac{L/S}{R} = \frac{L}{RS} \tag{1}$$

where σ is the electrical conductivity (in S/m), L is the length of sample (in m), and S is the cross-sectional area of the electrode (in m^2).

The temperature dependence of electrical conductivity in natural hydrous basalts was found to satisfy the Arrhenius relation, where

$$\sigma = \sigma_0 \exp(-\Delta H/kT). \tag{2}$$

Here, σ_0 is the pre-exponential factor (in S/m), ΔH is the activation enthalpy (in eV), and k is the Boltzmann constant (in eV/K). The activation enthalpy is pressure-dependent and behaves as follows:

$$\Delta H = \Delta U + P\Delta V \tag{3}$$

where ΔU is the activation energy (in eV) and ΔV is the activation volume (in cm^3/mol). The measured electrical conductivities from our experimental analysis are shown in Figs. 5–7.

Fig. 5 shows the electrical conductivity of the XW-1 basalt sample ($Cw = 0.62$ wt.%) over two heating–cooling cycles for $P = 2.0$ GPa and $T = 823$–1173 K. The electrical conductivities in the first heating cycle at low temperature are much lower than those obtained in the subsequent cycle, but this discrepancy decreases with increasing temperature and then the conductivity completely overlaps at 1173 K. The possible reason is that the initial sample was not cooled/crystallized at an oxygen fugacity fixed by Ni–NiO, such that during the first heating cycle, redox-induced compositional re-equilibrium (e.g., adjacent of relative ratio between Fe^{2+} and Fe^{3+} ions) due to the use of the Ni–NiO buffer was both effective and affected our conductivity measurements. Thus, electrical conductivities from the first heating cycle were excluded from the analysis. However, the first cooling cycle is in good agreement with the second heating–cooling cycle. In most cases, the obtained impedance spectra in the first cooling cycle were chosen to calculate the sample conductivity to ensure the accuracy and precision of the conductivity measurements.

Fig. 6 shows the influence of pressure on the electrical conductivity of the XW-1 basalt for $Wc = 0.62$ wt.% and $T = 823$–1173 K. To avoid the effect of gradual compaction on the measurement results, we measured the electrical conductivity of the sample for $P = 0.5$–2.0 GPa, at a pressure interval of 0.5 GPa. A slight decrease in electrical conductivity with increasing pressure was observed at constant temperature, and the conductivity decreased by about 0.25 Log unit with the pressure change from 0.25 to 2.0 GPa. The electrical conductivities for each pressure were fitted by Eq. (2), and the activation energy and activation volume were then calculated from Eq. (3); the results are summarized in Table 2.

Fig. 7 shows the electrical conductivities of the basalt samples along with the variation of water content for $P = 2.0$ GPa and $T = 823$–1173 K. The electrical conductivity dramatically increases as the water content in the sample increases. Each data set is fitted by Eq. (2), and the fitting parameters for the Arrhenius relation are listed in Table 3.
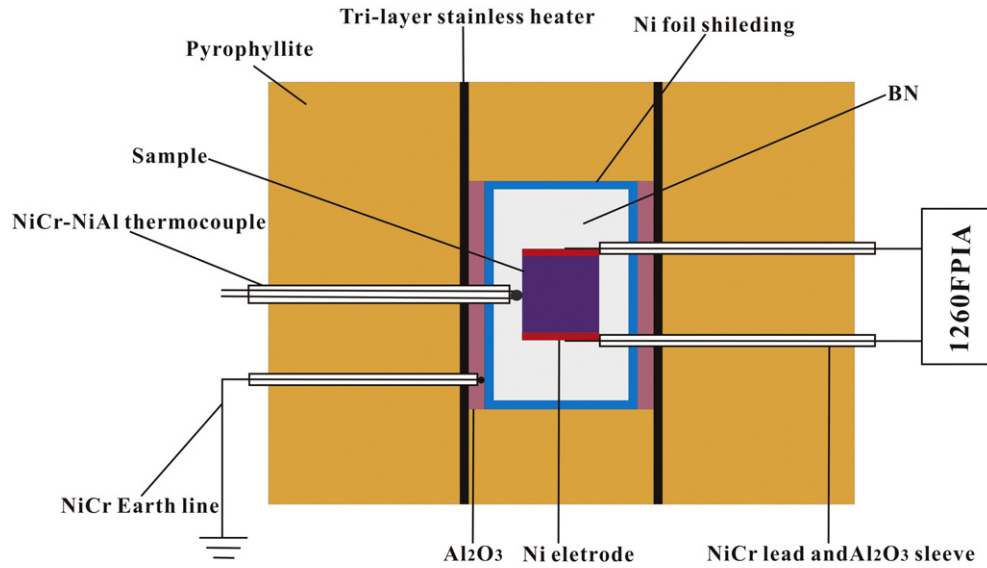
Fig. 2. Experimental setup for electrical conductivity measurements at high temperature and high pressure.

4. Discussion

4.1. Influence of pressure on electrical conductivity

Pressure has a weak influence on the electrical conductivity of hydrous basalts for $T = 823$–1173 K, as only a slight decrease in electrical conductivity with increasing pressure was observed (Fig. 6). We observed that the pre-exponential factors decrease and the activation enthalpy increases with increasing pressure, as shown in Table 2. From Eq. (3), $\Delta U = 0.86 \pm 0.14$ eV and $\Delta H = 1.43 \pm 0.25$ cm^3/mol, which reflect the weak influence of pressure on the electrical conductivity of hydrous basalts. This influence of pressure on electrical conductivity in basalts has been controversial until now, as relevant experimental reports are limited. Previous studies focused on the influence of partial melting on the electrical conductivity of synthetic or natural basalts (Ni et al., 2011; Pommier et al., 2010; Presnall et al., 1972; Scarlato

et al., 2004; Tyburczy and Waff, 1983). Tyburczy and Waff (1983) measured the electrical conductivity of molten Hawaiian tholeiite and Crater Lake andesite under conditions of $P = 0$–2.55 GPa and $T = 1473$–1673 K, and discovered that the electrical conductivity decreased with increasing pressure in both melts, with the tholeiite melt exhibiting a smaller pressure dependence than the andesitic melt. The electrical conductivity of the basaltic melts decreased by more than 0.1 Log unit from 0 to 0.85 GPa, and then remained approximately constant at higher pressures. Tyburczy and Waff (1983) further suggested that this discontinuity resulted from a change in melt structure rather than a conduction mechanism. Scarlato et al. (2004) conducted electrical conductivity measurements on two basaltic rocks (a lava flow and a mafic nodule) at $T = 673$–1373 K by complex impedance spectroscopy using a multi-anvil apparatus, and observed no pressure effects on conductivity for $P = 0.9$–1.5 GPa. Our range of activation enthalpy values for hydrous basalts ($\Delta H = 0.79$–0.90 eV) overlaps the experimental
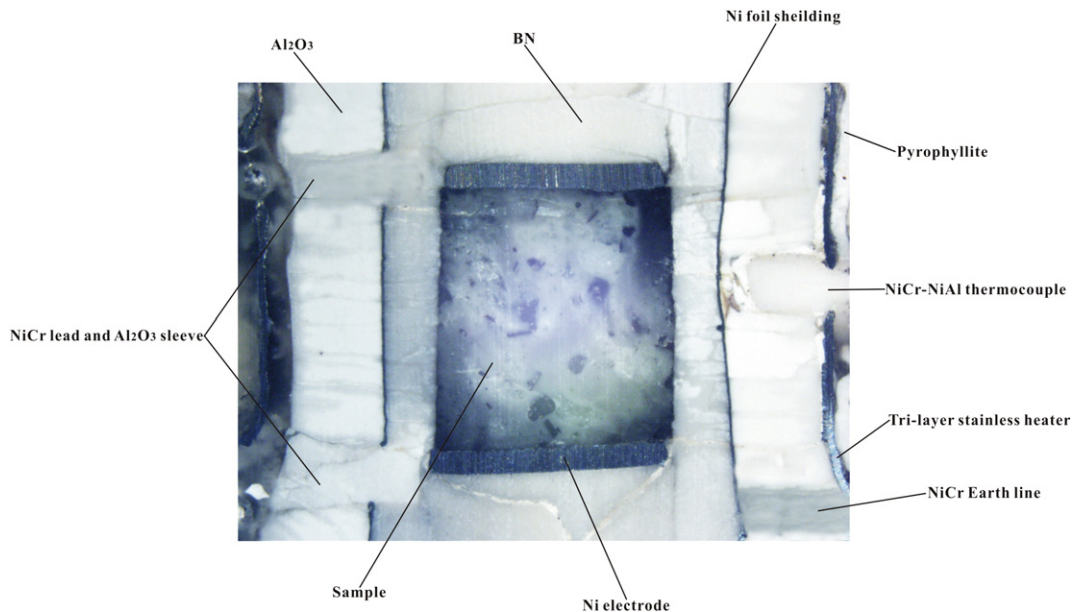

Fig. 3. A representative recovered experimental assembly after electrical conductivity for the XW-1 basalt at the pressure of 2.0 GPa.
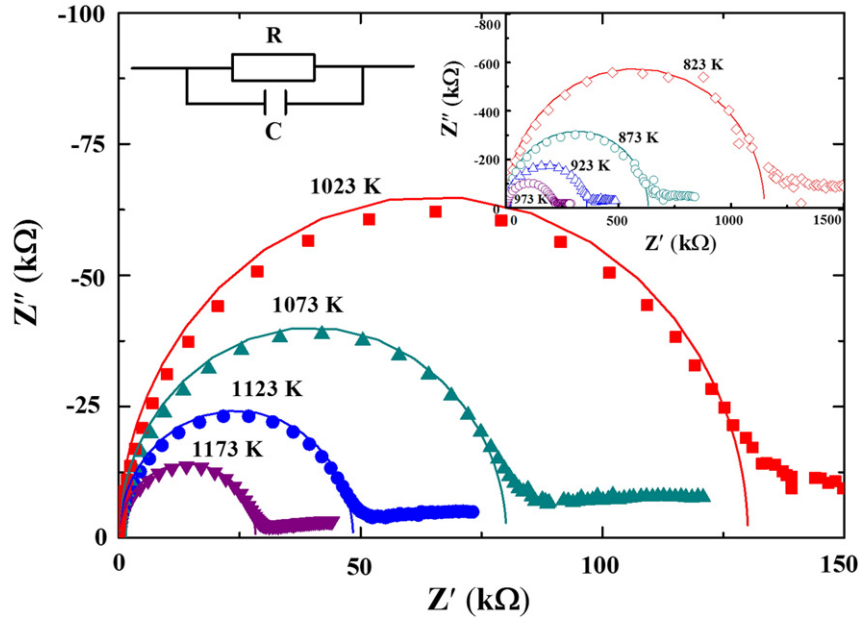
Fig. 4. Typical complex impedance spectra for natural hydrous Fe-bearing basalt (XW-1) in the frequency range from 10^{-2} Hz to 1 MHz obtained under the conditions of 2.0 GPa, 823–1173 K and a NNO oxygen buffer. Z' and Z'' represents the real part and imaginary part of complex impedance, respectively. An equivalent circuit of an R–C circuit element in parallel are used to fitting the impedance spectra in the high frequency region. The tail in the low frequency range, which is characteristic the electrical properties at the sample–electrode interface, is ruled out during data analysis process.

result for a lava flow ($\Delta H \sim 0.82$ eV) obtained by Scarlato et al. (2004). Pommier et al. (2010) examined the influence of temperature and oxygen fugacity (f_{O_2}) on the electrical conductivity of basaltic melts at room pressure, $T = 1473$–1673 K, and a range of oxygen partial pressures (10^{-8} to 2×10^{-1} bar) to explore the redox kinetics. They observed that f_{O_2} had a small but detectable effect on the conductivity of basalt melts, with similar redox rates that increased with temperature. At these higher temperatures, Pommier et al. (2010) calculated $\Delta H \sim 2.07$ eV, which is ~ 2.5 times larger than our result ($\Delta H \sim 0.86$ eV). They also proposed that high redox rates in basaltic melts result from the cooperative motion of cations and oxygen. Ni et al. (2011) reported the electrical conductivities of both H_2O-bearing ($Wc = 0$–6 wt.%) and CO_2-bearing (0.5 wt.% CO_2) basaltic melts at $P = 2.0$ GPa and $T = 1473$–1923 K by using impedance spectroscopy in a piston-cylinder apparatus. Although they did not consider the effect

of pressure on the electrical conductivity of basaltic melts, their results revealed that a 2% melt would account for the observed electrical conductivity in the seismic low-velocity zone for a typical mantle with $Wc = 125$ ppm and a bulk water partition coefficient between mineral and melt of 0.006.

4.2. Effect of water content on electrical conductivity

The electrical conductivities of our natural iron-bearing basalts display a strong dependence on water content, as demonstrated in Fig. 7. The electrical conductivity increases by approximately 1.5 orders of magnitude with increasing water content from 0.62 to 4.19 wt.% at each temperature point, while the activation enthalpy decreases from
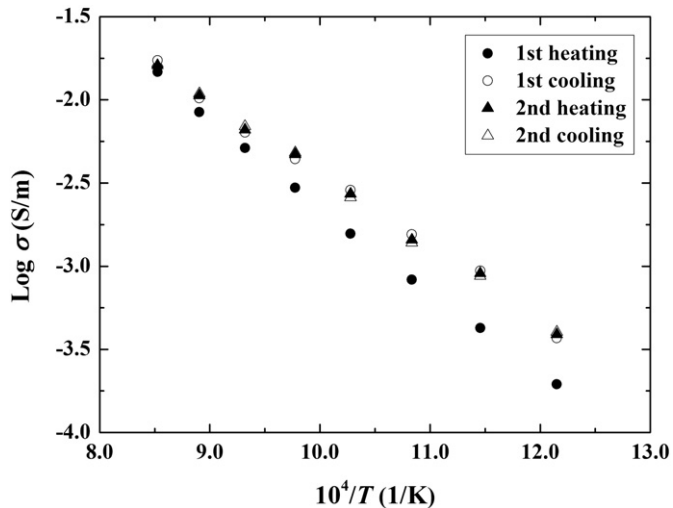

Fig. 5. Representative electrical conductivity results of XW-1 basalt sample ($C_W = 0.62$ wt.%) in two heating-cooling cycles between 823 and 1173 K at 2.0 GPa.
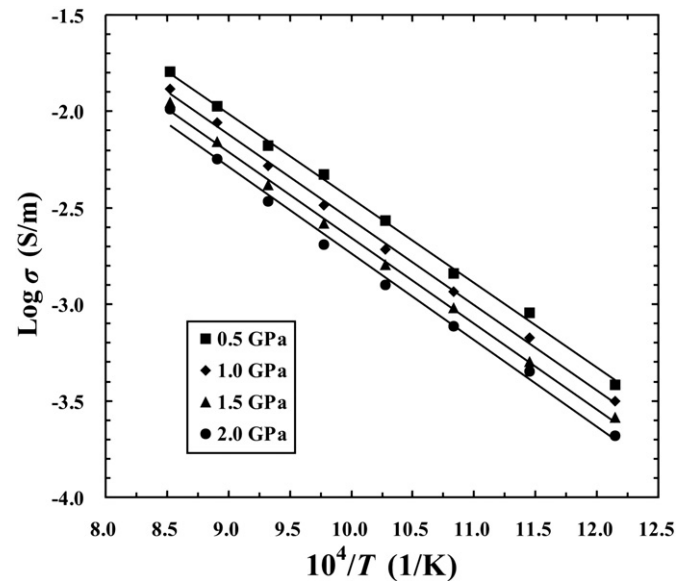

Fig. 6. The influence of pressure on the electrical conductivity of basalt (XW-1) with the 0.62 wt.% water content at the temperature range of 823–1173 K.
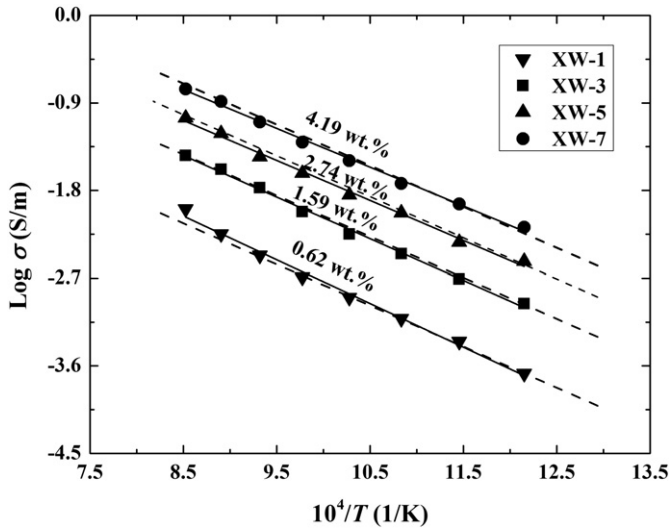
Fig. 7. The electrical conductivity of iron-bearing basalt with various water content under the conditions of 2.0 GPa and 823–1173 K. The numbers are the water content (in wt.%) in samples. The dashed lines represent the calculated results of hydrous basalts from Eq. (4) by using the fitting parameters shown in Table 4. These symbols indicate the raw data for each sample with different water contents. In here, there existed some deviations between the calculated results with our experimental obtained data, which is possibly due to the cooperation of mixed conduction mechanisms.

Table 3
Fitted parameters of Arrhenius relation for the electrical conductivity of basalt with different water contents.

Sample[#]	C_w (wt.%)	P (GPa)	T (K)	Log σ_0	σ_0 (S/m)	ΔH (eV)	γ^2
XW-1	0.62	2.0	823–1173	1.75	55.99	0.90	99.25
XW-3	1.59	2.0	823–1173	2.19	156.07	0.85	99.63
XW-5	2.74	2.0	823–1173	2.42	260.27	0.82	99.42
XW-7	4.19	2.0	823–1173	2.63	425.44	0.79	99.59

which is in close agreement with the experimental results. From Fig. 7, it is clear that there existed some deviations between the calculated results with our experimental obtained data, which is possibly due to the cooperation of mixed conduction mechanisms.

5. Geophysical implications

In situ laboratory measurements of the electrical conductivity of minerals and rocks at high temperatures and pressures are the most straightforward and effective method for constraining MT and geomagnetic depth sounding (GDS) inversion results. The electrical properties of minerals and rocks are highly sensitive to various factors, including temperature, pressure, oxygen fugacity, frequency, iron content, water content, grain boundary state, point defect chemistry, chemical composition, anisotropy of crystallographic axes, and electronic spin state transition. To evaluate laboratory-based conductivity results on a regional scale, a common transformation from the most volumetrically abundant constituent minerals to the most representative sophisticated rock assemblages at a certain depth is undertaken, on the basis of mineralogical composition, temperature distribution, and tectonic setting, in conjunction with petrological models of the constituent minerals of the deep earth (Dai et al., 2012; Pommier and Garnero, 2014). However, these laboratory results for an ideal rock may deviate from actual crustal and upper mantle materials, because the electrical conductivity of a rock defined as an aggregate of deep earth minerals may be restricted by a number of factors, such as grain boundary state, grain size, the heterogeneity of constituent minerals, water, and the iron partitioning coefficient.

We measured the electrical conductivity of hydrous basalts with different chemical compositions, at $P = 0.5$–2.0 GPa and $T = 823$–1173 K, using a Ni–NiO oxygen buffer to control the oxygen fugacity, and directly applied these results to establish a laboratory-based conductivity–depth profile. To establish such a profile for the middle to lower crust of the North China Craton (NCC), it is important to determine the distribution of the temperature field by converting the conductivity–temperature data into conductivity–depth data. By assuming a stationary continental lithosphere with no tectonic or volcanic activity in the crust, the internal temperature (T) of the earth field can be described by the numerical solution of the heat conduction equation (Čermák and Laštovičková, 1987):

$$T = T_0 + \left(\frac{Q}{k}\right)z - \left(\frac{A_0}{2k}\right)z^2 \qquad (5)$$

where T_0 is the surface temperature (in K), Q is the surface heat flow (in mW/m^2), z is the lithospheric layer depth (in km), k is the thermal conductivity (in W/mK), and A_0 is the lithospheric radiogenic heat productivity (in μW/m^3). Previous results on the elastic wave velocity and electrical conductivity of crustal amphibole from the Tarim Basin (China) at $P = 1.0$ GPa and $T = 523$–973 K indicate that the thermal calculation parameters for a representative region from the upper to lower crust of the NCC, over a depth range of 5 to 40 km, are $A_0 = 0.31$ μW/m^3, $k = 2.6$ W/mK, and $Q = 65$ mW/m^2 (Zhou et al., 2011).

Using the geothermal gradient models with $Q = 65$ mW/m^2 for the NCC and $Q > 60$ mW/m^2 for stable continental crust (Hu et al., 2000; Pollack et al., 1993) as a starting point, conductivity–depth profiles for

0.90 to 0.79 eV (Table 3). This observed increase in conductivity with water content is in agreement with previous studies that considered the main deep-earth minerals, such as hydrous pantellerite glass and dacitic volcanic rock (Laumonier et al., in press; Poe et al., 2012). These studies suggested that the mixed conduction mechanisms including small polaron hopping between Fe^{2+} and Fe^{3+} sites, alkali ions, and molecular water (H_2O) was the dominant conduction mechanism in the hydrogen-doped samples, where a slight reduction in activation enthalpy with increasing water content is connected to the cooperation of all of these sophisticated mixed conduction mechanisms (Poe et al., 2012).

We propose that the electrical conductivity of hydrous basalts follows the same trend as observed in some hydrous magmatic rocks and molten silicate glasses, such as pantellerite glass (Poe et al., 2012) and dacitic melts (Laumonier et al., in press). The electrical conductivities of hydrous basalts can also be expressed in terms of the charge species concentration dependence of the pre-exponential factor (A), which behaves in an Arrhenius relation, such that

$$\sigma = (A_1 + A_2 * C_w^\gamma) * \exp\left(\frac{-\Delta H_0 - \alpha C_w^\beta}{RT}\right) \qquad (4)$$

where r is a constant, ΔH_0 is the activation enthalpy observed at a very low water content, and α and β are empirical power-law constants. Our basalt data for different water contents were fit to Eq. (4) in a non-linear global least-squares sense and the fitting parameters listed in Table 4. The variations in electrical conductivity and activation enthalpy for hydrous basalts as a function of water content were also determined from Eq. (4), yielding electrical conductivity as a function of T^{-1} (Fig. 7),

Table 2
Fitting parameters for the electrical conductivity of XW-1 basalt sample with the 0.62 wt.% water content at different pressures.

Run no.	P (GPa)	T (K)	Log σ_0 (S/m)	ΔH (eV)	γ^2	ΔU (eV)	ΔV (cm^3/mol)
X1102	0.5	823–1173	1.93	0.87	99.76	0.86 ± 0.14	1.43 ± 0.25
X1108	1.0	823–1173	1.85	0.88	99.77		
X1112	1.5	823–1173	1.79	0.88	99.73		
X1120	2.0	823–1173	1.75	0.90	99.25		

Table 4
Fitting parameters obtained from the Eq. (4) for electrical conductivity of hydrous Fe-bearing basalt and comparison with the dominant constituent minerals of hydrous clinopyroxene and plagioclase by Yang et al. (2011, 2012).

Sample	A_1 (S/m)	A_2 (S/m)	ΔH_0 (eV)	r	α	β	Sources
Hydrous basalt	1.49 (12)	1.81 (6)	1.14 (7)	1.65 (3)	0.26 (9)	0.20 (9)	In this study
Hydrous clinopyroxene	3.56 ± 0.10		0.74 ± 0.01	1.13 ± 0.05	–	–	Yang et al. (2011)
Hydrous plagioclase	2.49 ± 0.14		0.80 ± 0.02	0.83 ± 0.06	–	–	Yang et al. (2012)

hydrous iron-bearing basalts have been obtained at $T = 423$–1173 K with a Ni–NiO solid buffer and a depth range of 5–40 km. Fig. 8 compares our laboratory-based conductivity–depth profiles with three separate geophysical MT results from (1) the magmatically active Axial Volcanic Ridge (AVR) along the Mid-Atlantic Ridge (Sinha et al., 1997), (2) the Zhangjiakou–Penglai tectonic zone in the NCC (Zhao et al., 1998), and (3) the transverse electric (TE, defined as the electric field along the strike and the magnetic field across the strike) and transverse magnetic (TM, defined as the electric field across the strike and the magnetic field along the strike) modes in the Northern Australian lithosphere (Heinson and White, 2005). The anomalous high-conductivity layers (HCL) under these representative stable continental crusts are available at conductivities of ~10^{-1} S/m and a depth range of 17–27 km in the NCC. Although our laboratory-based conductivity–depth profiles for hydrous iron-bearing basalts (for $Q = 65$ mW/m^2) will intersect with the stable continental crust from the MT observation data in the NNC at ~30–40 km depth, the AVR at ~22–40 km depth, and the TE model at ~15–28 km depth, the electrical conductivity of natural basalts with $Cw = 0.62$–4.19 wt.% does not account for the crustal high-conductivity anomaly in the Zhangjiakou–Penglai tectonic zone of the North China platform. Thus, our natural hydrous iron-bearing basalts may provide a potential lower limit and an important constraint on the MT results for the NCC, AVR and TE models.
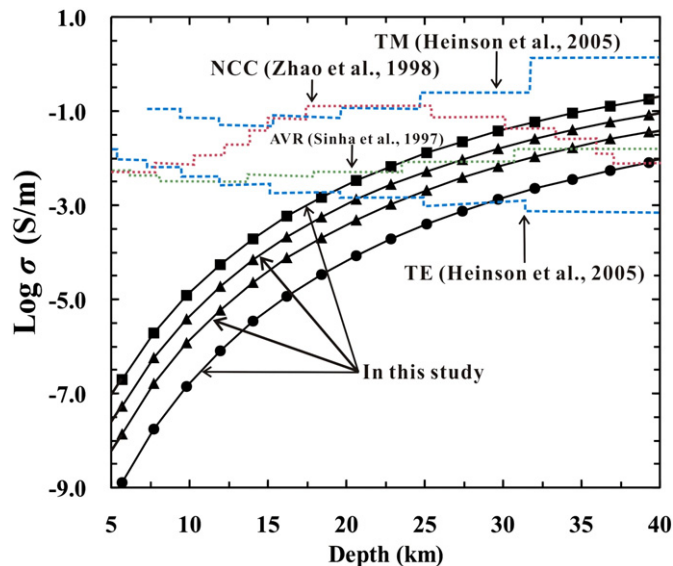

Fig. 8. Laboratory-based conductivity-depth profiles constructed from the data of natural hydrous Fe-bearing basalts and geothermal temperature gradient, and comparison with geophysically inferred field results in the mid-lower crust. The black solid lines represent the conductivity–depth profiles from the conductivity of samples at 2.0 GPa as described in the Fig. 7 and based on the surface heat flow of 65 mW/m^2 in North China Craton. The red, green and blue dashed lines stand for the magnetotelluric data derived from the region of the Zhangjiakou–Penglai tectonic zone in North China Craton (NCC) (Zhao et al., 1998), the magmatically active Axial Volcanic Ridge (AVR) in the Mid-Atlantic Ridge (Sinha et al., 1997), and as well as the transverse electric (TE, is defined as the electric filed along the strike and the magnetic field across the strike) and transverse magnetic (TM, is defined as the electric filed across the strike and the magnetic field along the strike) modes in Northern Australian lithosphere (Heinson and White, 2005), respectively.

As illustrated in Fig. 8, our electrical conductivities of hydrous iron-bearing basalts derived from laboratory data are lower than those of HCL inferred from the Zhangjiakou–Penglai tectonic zone in the NCC and the transverse magnetic model of the Northern Australian lithosphere; there exists no definitive mechanism to explain this discrepancy. Thus, a more comprehensive consideration of the influence factors that can produce crustal high electrical conductivity layers is required. Mathez et al. (2008) argued that the deposition of carbonaceous films results in an increase of electrical conductivity in the bulk Sioux quartzite due to an interconnected circuit on a micofracture network, implying that the change in the electrical properties of the rock is in direct response to brittle deformation. They also confirmed that the presence of interconnected carbon arrays along grain boundaries or along microfractures or megascopic thoroughgoing fractures may lead to this crustal high conductivity anomaly (Mathez et al., 1995; Roberts et al., 1999; Shankland et al., 1997). Ni et al. (2011) suggested that 0.3–2.0 wt.% of hydrous basaltic melt can account for the anomalous high-conductivity and low-velocity zone (LVZ), or at least the upper LVZ (70–110 km depth), under conditions of $P = 2.0$ GPa and $T = 1473$–1923 K. It has been suggested that all of these influencing factors, including partial melting (Ni et al., 2011; Pommier et al., 2010; Scarlato et al., 2004; Tyburczy and Waff, 1983), interconnected carbon arrays along grain boundaries or fracture surfaces (Mathez et al., 1995, 2008; Roberts et al., 1999; Shankland et al., 1997), water content (Ni et al., 2011), crystallographic anisotropy (Wang et al., 2010), the coexistence of other phases (Zhou et al., 2011), and the dehydration of rock-forming minerals (Fuji-ta et al., 2011) in crustal rock samples can produce HCL for a given lithospheric tectonic unit and can also be used to interpret the discrepancy in results obtained for the Zhangjiakou–Penglai tectonic zone in the NCC and the TM model Northern Australian lithosphere, and our current results.

In summary, we conclude that the electrical conductivities of four natural basalts, with 0.62–4.19 wt.%, can be applied to interpret MT results from these typical crustal tectonic units for the NNC, AVR and TE models at a corresponding depth range. It is noted, however, that further studies on the electrical conductivities of other coexisting phases in hydrous rocks are needed to account for high-conductivity anomalies in the crust.

Acknowledgments

References

Bagdassarov, N., 2011. Phase transitions in CsHSO$_4$ up to 2.5 GPa: impedance spectroscopy under pressure. J. Phys. Chem. Solids 72, 236–244.
Bagdassarov, N., Delépine, N., 2004. α-β inversion in quartz from low frequency electrical impedance spectroscopy. J. Phys. Chem. Solids 65, 1517–1526.

Bagdassarov, N., Golabek, G., Solferino, G., Schmidt, M., 2009. Constraints on the Fe-S melt connectivity in mantle silicates from electrical impedance measurements. Phys. Earth Planet. Inter. 177, 139–146.

Bagdassarov, N., Batalev, V., Egorova, V., 2011. State of lithosphere beneath Tien Shan from petrology and electrical conductivity of xenoliths. J. Geophys. Res. 116, B01202. http://dx.doi.org/10.1029/2009JB007125.

Bedrosian, P.A., 2007. MT+, integrating magnetotellurics to determine earth structure, physical state, and processes. Surv. Geophys. 28, 121–167.

Čermák, V., Laštovičková, M., 1987. Temperature profiles in the earth of importance to deep electrical conductivity models. Pageoph 25, 255–284.

Dai, L., Karato, S., 2014. High and highly anisotropic electrical conductivity of the asthenosphere due to hydrogen diffusion in olivine. Earth Planet. Sci. Lett. 408, 79–86.

Dai, L., Li, H., Hu, H., Shan, S., Jiang, J., Hui, K.S., 2012. The effect of chemical composition and oxygen fugacity on the electrical conductivity of dry and hydrous garnet at high temperatures and pressures. Contrib. Mineral. Petrol. 163, 689–700.

Dai, L., Li, H., Hu, H., Shan, S., Jiang, J., Hui, K., 2013. Electrical conductivity of $Alm_{82}Py_{15}Grs_3$ almandine-rich garnet determined by impedance spectroscopy at high temperatures and high pressures. Tectonophysics 608, 1086–1093.

Dai, L., Hu, H., Li, H., Shan, S., Jiang, J., Hui, K., 2014. Effects of temperature, pressure and chemical composition on the electrical conductivity of granite and its geophysical implications. Am. Mineral. 99, 1420–1428.

Fuji-ta, K., Katsura, T., Tainosho, Y., 2004. Electrical conductivity measurement of granulite under mid- to lower crustal pressure-temperature conditions. Geophys. J. Int. 157, 79–86.

Fuji-ta, K., Katsura, T., Ichiki, M., Matsuzaki, T., Kobayashi, T., 2011. Variations in electrical conductivity of rocks above metamorphic conditions. Tectonophysics 504, 116–121.

Gasc, J., Brunt, F., Bagdassarov, N., Morales-Flórez, V., 2011. Electrical conductivity of polycrystalline $Mg(OH)_2$ at 2 GPa: effect of grain boundary hydration–dehydration. Phys. Chem. Miner. 38, 543–556.

Heinson, G., White, A., 2005. Electrical resistivity of the northern Australian lithosphere: crustal anisotropy or mantle heterogeneity? Earth Planet. Sci. Lett. 232, 157–170.

Hu, S., He, L., Wang, J., 2000. Heat flow in the continental area of China: a new data set. Earth Planet. Sci. Lett. 179, 407–419.

Hu, H., Li, H., Dai, L., Shan, S., Zhu, C., 2011. Electrical conductivity of albite at high temperatures and high pressures. Am. Mineral. 96, 1821–1827.

Hu, H., Li, H., Dai, L., Shan, S., Zhu, C., 2013. Electrical conductivity of alkali feldspar solid solutions at high temperatures and high pressures. Phys. Chem. Miner. 40, 51–62.

Hu, H., Dai, L., Li, H., Jiang, J., Hui, K., 2014. Electrical conductivity of K-feldspar at high temperature and high pressure. Mineral. Petrol. 108, 609–618.

Huebner, J.S., Dillenburg, R.G., 1995. Impedance spectra of hot, dry silicate minerals and rock: qualitative interpretation of spectra. Am. Mineral. 80, 46–64.

Laumonier, M., Gaillard, F., Sifre, D., 2014. The effect of pressure and water concentration on the electrical conductivity of dacitic melts: implication for magnetotelluric imaging in subduction area. Chem. Geol. http://dx.doi.org/10.1016/j.chemgeo.2014.09.019 (in press).

Li, H., Xie, H., Guo, J., Zhang, Y., Xu, Z., 1999. In situ control of oxygen fugacity at high temperature and high pressure. J. Geophys. Res. 104, 29439–29451.

Liu, S., Hu, R., Feng, C., Gao, S., Feng, G., Qi, Y., Wang, T., Coulson, I.M., Yang, Y., Yang, C., 2012. U-Pb zircon age, geochemical and Sr-Nd isotopic constraints on the age and origin of the granodiorites in Guilong, Southeastern Yunnan province, southern China. Open J. Geol. 2, 229–240.

Mathez, E., Duba, A., Peach, C., Léger, A., Shankland, T.J., Plafker, G., 1995. Electrical conductivity and carbon in metamorphic rocks of the Yukon-Tanana, Alaska. J. Geophys. Res. 100, 10187–10196.

Mathez, E., Roberts, J.J., Duba, A., Kronenberg, A., Karner, S., 2008. Carbon deposition during brittle rock deformation: changes in electrical properties of fault zones and potential geoelectric phenomena during earthquakes. J. Geophys. Res. 113, B12201. http://dx.doi.org/10.1029/2008JB005798.

Maumus, J., Bagdassarov, N., Schmeling, H., 2005. Electrical conductivity and partial melting of mafic rocks under pressure. Geochim. Cosmochim. Acta 69, 4703–4718.

Ni, H., Keppler, H., Behrens, H., 2011. Electrical conductivity of hydrous basaltic melts: implications for partial melting in the upper mantle. Contrib. Mineral. Petrol. 162, 637–650.

Parkhomenko, E., Bondarenko, A., 1986. Electrical conductivity of rocks at high pressures and temperatures. Transl. into English of the book 1. pp. 1–5.

Poe, B., Romano, C., Genova, D., Behrens, H., Scarlato, P., 2012. Mixed electrical conduction in a hydrous pantellerite glass. Chem. Geol. 320–321, 140–146.

Pollack, H.N., Hurter, S.J., Johnson, J.R., 1993. Heat flow from the Earth's interior: analysis of the global data set. Surv. Geophys. 31, 267–280.

Pommier, A., Garnero, E.J., 2014. Petrology-based modeling of mantle melt electrical conductivity and joint interpretation of electromagnetic and seismic results. J. Geophys. Res. 119. http://dx.doi.org/10.1002/2013JB010449.

Pommier, A., Gaillard, F., Pichavant, M., 2010. Time-dependent changes of the electrical conductivity of basaltic melts with redox state. Geochim. Cosmochim. Acta 74, 1653–1671.

Presnall, D.C., Simmons, C.L., Porath, H., 1972. Changes in electrical conductivity of a synthetic basalt during melting. J. Geophys. Res. 77, 5665–5672.

Roberts, J.J., Tyburczy, J.A., 1991. Frequency dependent electrical properties of polycrystalline olivine compacts. J. Geophys. Res. 96, 16205–16222.

Roberts, J.J., Duba, A., Mathez, A., Shankland, T.J., Kinzler, R., 1999. Carbon-enhanced electrical conductivity during fracture of rocks. J. Geophys. Res. 104, 737–747.

Scarlato, P., Poe, B.T., Freda, C., 2004. High-pressure and high-temperature measurements of electrical conductivity in basaltic rocks from Mount Etna, Sicily, Italy. J. Geophys. Res. 10, B02210. http://dx.doi.org/10.1029/2003JB002666.

Selway, K., 2014. On the causes of electrical conductivity anomalies in tectonically stable lithosphere. Surv. Geophys. 35, 219–257.

Selway, K., Yi, J., Karato, S., 2014. Water content of the Tanzanian lithosphere from magnetotelluric data: implications for cratonic growth and stability. Earth Planet. Sci. Lett. 388, 175–186.

Shan, S., Wang, R., Guo, J., Li, H., 2007. Pressure calibration for the sample cell of YJ-3000 t multi-anvil press at high-temperature and high-pressure. Chin. J. High Press. Phys. 21, 367–372.

Shankland, T.J., Duba, A., Mathez, E., Peach, C., 1997. Increase of electrical conductivity with pressure as an indicator of conduction through a solid phase in midcrustal rocks. J. Geophys. Res. 102, 14741–14750.

Sinha, M.C., Navin, D., MacGregor, L., Constable, S., Peirce, C., White, A., Heinson, G., Inglis, M., 1997. Evidence for accumulated melt beneath the slow-spreading Mid-Atlantic Ridge. Phil. Trans. R. Soc. Lond. A 355, 233–253.

Tyburczy, J., Waff, H., 1983. Electrical conductivity of molten basalt and andesite to 25 kilobars pressure: geophysical significance and implications for charge transport and melt structure. J. Geophys. Res. 88, 2413–2430.

Wang, D., Li, H., Yi, L., Matsuzaki, T., Yoshino, T., 2010. Anisotropy of synthetic quartz electrical conductivity at high pressure and temperature. J. Geophys. Res. 115, B09211. http://dx.doi.org/10.1029/2009JB006695.

Watson, H., Roberts, J., Tyburczy, J., 2010. Effect of conductive impurities on electrical conductivity in polycrystalline olivine. Geophys. Res. Lett. 37, L02302. http://dx.doi.org/10.1029/2009GL041566.

Xia, Q., Liu, J., Liu, S., Kovács, I., Feng, M., Dang, L., 2013. High water content in Mesozoic primitive basalts of the North China Craton and implications on the destruction of cratonic mantle lithosphere. Earth Planet. Sci. Lett. 361, 85–97.

Xu, J., Zhang, Y., Hou, W., Xu, H., Guo, J., Wang, Z., Zhao, H., Wang, R., Huang, E., Xie, H., 1994. Measurements of ultrasonic wave velocities at high temperature and high pressure for window glass. High Temp. High Press. 26, 375–384.

Yang, X., Keppler, H., McCammon, C., Ni, H., Xia, Q., Fan, Q., 2011. Effect of water on the electrical conductivity of lower crustal clinopyroxene. J. Geophys. Res. 116, B04208. http://dx.doi.org/10.1029/2010JB008010.

Yang, X., Keppler, H., McCammon, C., Ni, H., 2012. Electrical conductivity of orthopyroxene and plagioclase in the lower crust. Contrib. Mineral. Petrol. 163, 33–48.

Zhao, G., Liu, G., Zhan, Y., Jiang, Z., Liu, T., Tang, J., Wang, J., Li, W., Liang, J., 1998. The structure of the crust and upper mantle for the Zhangbei-Shangyi seismic area and its neighboring region. Seismol. Geol. 155–189.

Zhou, W., Fan, D., Liu, Y., Xie, H., 2011. Measurements of wave velocity and electrical conductivity of an amphibolite from southwestern margin of the Tarim Basin at pressures to 1.0 GPa and temperatures to 700 °C: comparison with field observations. Geophys. J. Int. 187, 1393–1404.